中国光学（中英文） Chinese Optics 核心期刊

Co-phasing method for sparse aperture optical systems based on multichannel fringe tracking

AN Qi-chang, WANG Kun, LIU Xin-yue, LI Hongwen, ZHU Jiakang

Citation:
AN Qi-chang, WANG Kun, LIU Xin-yue, LI Hongwen, ZHU Jiakang. Co-phasing method for sparse aperture optical systems based on multichannel fringe tracking[J]. *Chinese Optics*, In press. doi: 10.37188/CO.EN-2024-0002
安其昌, 王, 刘欣悦, 李洪文, 朱嘉康. 基于多路条纹跟踪的稀疏孔径光学系统共相方法[J]. 中国光学, 优先发表. doi: 10.37188/CO.EN-2024-0002

View online: https://doi.org/10.37188/CO.EN-2024-0002

Articles you may be interested in

Cophasing error of the Golay3 sparse aperture imaging system
Golay3稀疏孔径成像系统共相误差研究
Chinese Optics. 2023, 16(4): 833 https://doi.org/10.37188/CO.2022-0203

A new co-phasing detection technology of a segmented mirror based on broadband light
基于宽波段光源拼接镜新型共相检测技术研究
Chinese Optics. 2022, 15(4): 797 https://doi.org/10.37188/CO.2021-0234

Assembling and test method for main focus survey telescope based on curvature sensing
基于曲率传感的主焦巡天望远镜集成检测方法
Chinese Optics. 2023, 16(3): 535 https://doi.org/10.37188/CO.2023-0010

Overview of key technologies for segmented mirrors of large-aperture optical telescopes
大口径光学望远镜拼接镜面关键技术综述
Chinese Optics. 2022, 15(5): 973 https://doi.org/10.37188/CO.2022-0109

Sub region curvature sensing method for survey telescope with larger aperture
大口径巡天望远镜分区域曲率传感方法研究
Chinese Optics. 2023, 16(2): 358 https://doi.org/10.37188/CO.2022-0117

Aberration coupling characteristics of axial and lateral misalignments of off-axis three-mirror telescopes
离轴三反望远镜轴向与横向失调量像差耦合特性
Chinese Optics. 2022, 15(4): 747 https://doi.org/10.37188/CO.2021-0164

文章编号　2097-1842(xxxx)x-0001-14

Co-phasing method for sparse aperture optical systems based on multichannel fringe tracking

AN Qi-chang[1,2,3 *], WANG Kun[1,2,3], LIU Xin-yue[1,2,3], LI Hongwen[1,2,3], ZHU Jiakang[1,2,3]

（1. *Changchun Institute of Optical Precision Machinery and Physics*, *Chinese Academy of Sciences*, *Changchun*, *Jilin* 130033, *China*;

2. *University of Chinese Academy of Sciences*, *Beijing* 100039, *China*;

3. *Jilin Key Laboratory of Intelligent Wavefront Sensing and Control*, *Changchun*, *Jilin* 130033, *China*）

* *Corresponding author*, *E-mail*: *anjj@mail.ustc.edu.cn*

Abstract: To realize effective co-phasing adjustment in large-aperture sparse-aperture telescopes, a multichannel stripe tracking approach is employed, allowing simultaneous interferometric measurements of multiple optical paths and circumventing the need for pairwise measurements along the mirror boundaries in traditional interferometric methods. This approach enhances detection efficiency and reduces system complexity. Here, the principles of the multibeam interference process and construction of a co-phasing detection module based on direct optical fiber connections were analyzed using wavefront optics theory. Error analysis was conducted on the system surface obtained through multipath interference. Potential applications of the interferometric method were explored. Finally, the principles of the multipath interference process were experimentally revealed. Evidently, flat-field calibration and incoherent digital synthesis enhanced the fringe contrast to more than 0.4, with the dynamic range exceeding 10 times the working center wavelength (1 550 nm). Moreover, a resolution better than one-tenth of the working center wavelength (1 550 nm) was achieved. Simultaneous three-beam interference can be achieved, leading to a 50% improvement in detection efficiency. This method can effectively enhance the efficiency of sparse aperture telescope co-phasing, meeting the requirements for observations of 8–10 m telescopes. This study provides a technological foundation for observing distant and faint celestial objects.

Key words: stripe tracking; wavefront aberration; sparse aperture telescope; co-phasing adjustment

---

收稿日期:xxxx-xx-xx; **修订日期:**xxxx-xx-xx

基金项目:中文基金

This work was supported by the National Natural Science Foundation of China (No. 12373090, No.12133009), the Youth Innovation Promotion Association of the Chinese Academy of Sciences (No. 2020221)

基于多路条纹跟踪的稀疏孔径光学系统共相方法

安其昌[1,2,3*], 王　鹞[1,2,3], 刘欣悦[1,2,3], 李洪文[1,2,3], 朱嘉康[1,2,3]
（1. 中国科学院长春光学精密机械与物理研究所, 吉林长春 130033；
2. 中国科学院大学, 北京 100039；
3. 吉林省智能波前传感与控制重点实验室, 吉林长春 130033）

摘要: 为了实现大口径稀疏孔径望远镜的有效共相调整, 采用了多通道条纹跟踪方法, 允许同时进行多个光路的干涉测量, 避免了传统干涉方法中沿镜面边界进行成对测量的需要, 从而实现了检测效率的提高与系统复杂性的降低。在这里, 我们使用光学波前理论分析了多光束干涉过程的原理和基于光纤直接连接的共相检测模块构造, 并对通过多路径干涉获得的系统面型进行了误差分析, 探索了干涉方法的潜在应用。最后, 通过实验揭示了多路径干涉过程的原理, 得到了平场校准和非相干数字合成能够将条纹对比度提高到超过 0.4, 并且动态范围超过工作中心波长(1 550 nm)的 10 倍, 实现了比工作中心波长(1 550 nm)好的分辨率。三光束干涉的同时实现提高了 50% 的检测效率, 从而有效提高稀疏孔径望远镜的共相效率, 满足了 8-10 米望远镜的观测要求, 为观察遥远和暗淡的天体提供了技术基础。

关　键　词: 条纹跟踪; 波相差; 稀疏孔径望远镜; 共相调整
中图分类号:　　**文献标志码:** A　　**doi:** 10.37188/CO.EN-2024-0002　　**CSTR:** 32171.14.CO.EN-2024-0002

1 Introduction

Large-aperture sparse-aperture telescopes (LASATs) represent a sparse aperture high-resolution optical system, usually with wavelength-level measurement and driving capabilities. They boast high resolution and light-gathering capacity, and have achieved breakthroughs in fields demanding high detection resolution and sensitivity, such as observations of the first cosmic light and near-Earth asteroid detection[1-3]. In ground-based observations, each mirror of the LASAT can independently perform detection tasks. This approach reduces the technological risk and shortens the number of scientific output cycles. The Giant Magellan Telescope in the United States comprises seven individual mirrors, each with a diameter of 8.4 m. These mirrors were combined to form the final telescopic system with an effective aperture of 30 m. By sequentially adding seven primary mirrors to the telescope, the total detection time of the system was effectively increased. Moreover, independent observations have been conducted without utilizing all seven primary mirrors. The Large Binocular Telescope comprises two telescopes, each with an aperture of 8 m. Based on the principles of planetary interferometry, celestial objects can be detected with high resolution and sensitivity in terms of angular radius measurements. This technology allows precise observation of space targets[4-7].

In space exploration, sparse-aperture telescopes are advantageous owing to their volume and weight. By launching the telescope independently or collectively into orbit, the sparse-aperture telescope can achieve independent observations as well as an on-orbit assembly for integrated observations (by synthesizing multiple telescopes into an equivalent single telescope). This reduces launch costs and enhances mission safety. The Gaia space telescope consists of two optical systems[8], which can be regarded as generalized sparse-aperture systems. Each optical system comprises five reflective mirrors, with the rear mirror serving as a beam-combining system. Gaia enables large-scale imaging surveys of the Milky Way galaxy through precise alignment of the two systems. Similar space-based optical survey instruments, such as the Chinese Space Station Tele-

scope, can contribute to the elucidation of physical laws under extreme conditions by considering multimessenger observations. These instruments are critical for various applications, including multiband photometric surveys, multiband variability, spectral signal analysis, and the discovery of novel transient sources, such as supernovae, intermediate-mass black holes, and tidal disruption events involving binary black holes.

To achieve the equivalence of a single continuous mirror in the LASAT, the following two adjustments are required: co-focus and co-phase. The co-focus adjustment process can be treated as a coupling movement between the defocused and focal plane spots. For a spherical mirror, because of the infinite number of optical axes, the co-focus position of the primary mirror is selected to be within the adjustment range of the secondary mirror or corrective mirror group. For nonspherical segmented mirrors, the inclination of the optical axes between the segments introduces additional off-axis aberrations, such as astigmatism and coma, and a unique co-focus position deviates from, which may result in system aberrations at each image point when used as the reference point for co-focus measurement. Moreover, for a multisegmented mirror with multiple annular zones, a partial compensatory relationship exists between the variation in the radius of curvature of each annular zone and the axial defocus. Although this may have a relatively minor impact on the energy detection, it is critical for precise astronomical observations. In these cases, adjustments can be made by measuring high-order spherical aberrations to achieve fine-tuning and enhance the accuracy of the observations. With the achievement of a common focus as a foundation, LASAT requires the implementation of co-phase maintenance, which involves the following two stages: 1) adjustment of errors to within one wavelength (coarse co-phase), and 2) further adjustment of these errors within one wavelength to meet the imaging requirements of the system. Currently, dispersion fringe sensors are primarily used as coarse sensors in LASATs. However, these sensors not only encounter non-common path aberrations but also face challenges in effectively integrating with the telescope owing to the volume and mass constraints associated with the interferometric optical path constructed using bulk optical elements[9-11]. Narrowband interference methods are often employed for fine co-phase adjustments by utilizing the interference fringes created by the mask templates at the junctions of the sub-mirrors. Currently, the Keck telescope uses a two-point interference method to generate one-dimensional interference fringes. Conventional geometric shape measurement methods typically do not satisfy the accuracy requirements for phase detection. Therefore, optical interference methods should be employed to detect submicrometer-level step errors between the mirror surfaces.

Compared to ground-based telescopes such as KECK, the James Webb Telescope, despite its fewer mirrors and broader wavelength band, utilizes a universal iterative measurement based on focal-plane image assessments. This system requires an optical path that utilizes significant space in the backend[13]. Unlike the phased iterative measurement method of the James Webb Telescope, which employs numerous bulk optical elements, this approach enhances the light throughput of the system. This paves the way for universal phase measurements in the forthcoming generation of 20-m space splicing telescopes. Although these telescopes have more mirrors, current methods are not sufficiently efficient[14].

Ground-based telescopes, such as the European Extremely Large Telescope and the American Thirty Meter Telescope, utilize interferometry with free-space-combined optical elements by employing pairwise interference. Because only two channels of measurement can be performed at a time, this method has a lower measurement efficiency than ours. In addition, uniform calibration is required to address errors between channels, includ-

ing intensity attenuation, phase distortion, visibility differences, detector response, and noise. The proposed technique employs multi-channel interference, which significantly enhances both efficiency and accuracy[15].

Furthermore, a multiwavelength channel spectral method was used to achieve an accurate alignment between the coarse- and fine-phase processes, and the step errors between the submirrors near the working center wavelength were reduced. A multibeam interference approach was used for cooperative phase detection in sparse-aperture systems. A multipath fringe-tracking technique was employed to simultaneously acquire the phase differences between different paths, and aperture coding was used to achieve phase detection for different submirrors and positions. This approach enables rapid, accurate, and high-throughput system-wide phase sensing and control.

This paper introduces an innovative approach for the co-phasing detection of large-aperture segmented telescopes using methods rooted in astronomical photonics[16-18]. These methods can significantly reduce the volume and weight of a system while enhancing its environmental adaptability. Ground-based systems mitigate the effect of airflow on optical imaging paths. Space telescopes have substantially reduced weight and power consumption. Furthermore, the high integration of astronomical photonics and precise alignment of the system have paved the way for multipath interference and fringe tracking measurement techniques. This approach minimizes non-common optical path aberrations from various parallel path measurements. Consequently, it boosts detector utilization and effectively reduces the complexity and cost of co-phasing systems. As aspirations for large-aperture telescopes expand, the backend focal plane space becomes increasingly scarce. Astronomical photonics methods offer a solution that enables a reduction in the system volume and the capability to adeptly fold optical paths. This leads to an improved measurement efficiency and a decreased launch weight.

Section 2 presents the fundamental principles of fringe tracking, followed by an analysis of the phase-detection accuracy using interferometry in Section 3, along with a description of the detection architecture and process. Section 4 presents the verification of the phase-detection process in various modes, thereby providing a comprehensive understanding of the principles.

2 Materials and methods

2.1 Basic principles of multichannel fringe tracking

The fundamental principle of fringe tracking involves the extraction of the actual phase information of a system by analyzing the interference fringes and rapidly adjusting the phase to maintain the stability of large-aperture segmented mirrors. Hence, for both perception and control, the frequency must be higher than the changes in the fringe positions caused by external disturbances. The basic principles of fringe sampling and perception are illustrated in Fig. 1. In this figure, ABCD represents the sampling position intensity. The difference in the light intensity between A and D represents the visibility of the system fringes. The light intensities at different sampling positions were determined using the two input light intensities and phases of the system. Between the low- and high-light intensities, there must be a special intermediate point to suppress sampling noise and build a light intensity benchmark.

The direct extraction of fringe positions is affected by local variations in light intensity and noise, especially in the case of multibeam interference. The envelopes generated by multiple beams are complex and impact fringe extraction. Here, a theoretical analysis was employed to construct an interference intensity model using the example of three beams, for a detailed expansion. Simultaneously, the overall wavefront information was con-

structed by acquiring the local height differences at the boundaries and sampling the spatial frequency. Subsequently, the postures of the individual submirrors in a sparse aperture were obtained through plane fitting (where positional errors are passively maintained by the system accuracy).

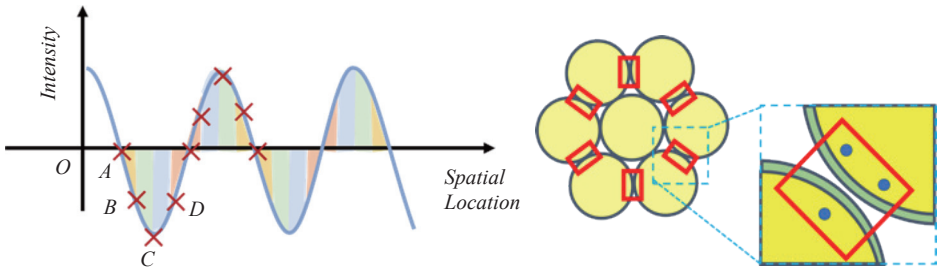

(a) (b)

Fig. 1 Fundamental principles of fringe sampling. (a) System light-intensity sampling position and (b) sparse-aperture boundary multi-point sampling position.

In the actual detection process, stable interference is formed through a photon transmission path constructed using optical fibers and spatial filters[19-20]. The intensities generated from the three-path interference are represented by Eq. (1).

$$I_i^N = \left[\sum_{j=1}^{N}|E_{ij}|^2 - \sum_{k,l=1}^{N} 2|E_{ik}||E_{il}|\sin\left(\frac{2\pi}{\lambda_i}\left(\vec{\delta}_{kli}\right)\right)\right], \quad (1)$$

where $|E_{ij}|^2$ represents the respective light intensity of each path; λ is the wavelength of the channel spectral center; j denotes the interfering beams of light; N is the total, δ_{kj} is the optical path difference (OPD) between the two paths of the system; and λ_i is a known value. Optical fiber connections enable aperture reconfiguration, facilitating integrated interferometry without altering the optical path of the original imaging system. This integration is achieved using an aperture coding system. Flexibility in adjusting the interference in each path is accomplished, and the final interferogram of the three-path interference is processed using phase coherence to determine its circularity. The architecture of the coherent interference detection system of LASAT is illustrated in Fig. 2.

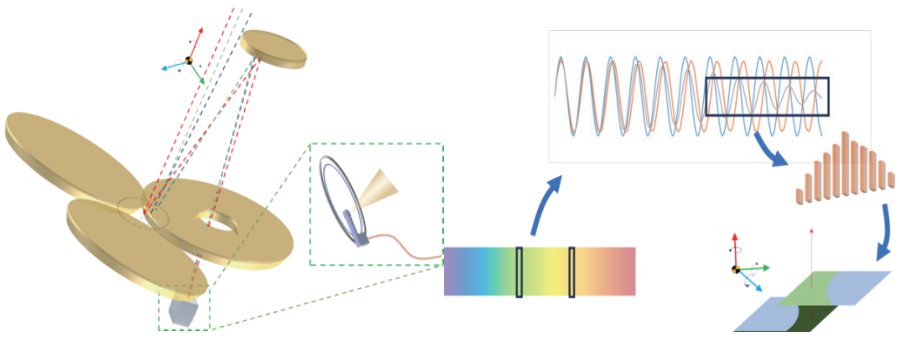

(a) (b)

Fig. 2 Multilevel co-phasing of a large-aperture sparse optical system. (a) Architecture of optical collection and (b) perception and control of the local step difference based on multiwavelengths.

In this study, a theoretical analysis was performed for the synthesis of three beams. The expression of beam intensity under a single-channel spectrum was obtained, and the system error was smoothly suppressed through beam phase closure.

System detection throughput can be effectively enhanced by employing a multilevel fringe-tracking system. Based on this, the efficiency of wavefront sampling and the resulting final pixel resolution of the target surface were analyzed. By selecting three

channels and substituting in Eq. (1) yields

$$I_i^3 = \left[|E_{i1}|^2 + |E_{i2}|^2 + |E_{i3}|^2 - 2|E_{i1}||E_{i2}|\sin\left(\frac{2\pi}{\lambda_i}\left(\vec{\delta}_{12i}\right)\right) - 2|E_{i3}||E_{i1}|\sin\left(\frac{2\pi}{\lambda_i}\left(\vec{\delta}_{13i}\right)\right) - 2|E_{i3}||E_{i2}|\sin\left(\frac{2\pi}{\lambda_i}\left(\vec{\delta}_{23i}\right)\right)\right], \quad (2)$$

where $|E_{i1}|^2$, $|E_{i2}|^2$, and $|E_{i3}|^2$ are the light intensities of each of the three channels; λ_i is the wavelength of the channel spectral center; and i1, i2, and i3 denote the interfering beams. Because of the phase-closure property of three-channel light interference, three-channel light rays can be assumed to oscillate in trace amounts near their common average position. Using small-angle approximation and intensity $|E_i|$ for each channel, the expression can be simplified as follows:

$$I_i^3 = \left[3|E_i|^2 - 2|E_i|^2 \frac{2\pi}{\lambda_i}\left(\vec{\delta}_{12i} + \vec{\delta}_{13i} + \vec{\delta}_{23i}\right)\right] \quad . \quad (3)$$

By performing interference synthesis on the three beams, the phase difference between the two beams can be obtained, whereas the average phase difference among the three beams can be determined. Finally, the absolute phase difference is obtained using the phase-closure principle. Assuming that route 3 measures its phase difference relative to routes 1 and 2, whereas routes 1 and 2 remain unchanged, the interference phase measurement error introduced by the baseline changes can be eliminated by subtracting the measured phase differences of routes 1 and 2 from the obtained results. Two beams of interfering light were used to establish a reference for calculating the phase in multilevel interferometry.

Using a single wavelength for interference, the dynamic detection range of the system can be expanded using the channel spectrum. The multiwavelength sampling process is shown in Fig. 2(a), where the system acquires beams of multiple wavelengths that ultimately converge on the focal plane. Photonic devices were used on the focal plane for collection, and integrated interference was applied to the backend.

The fringe interference process based on the channel spectrum is illustrated in Fig. 2(b). The interference fringes in the two narrow bandwidths eventually form a periodic light-intensity distribution. This period can be used to effectively expand the dynamic range of the measurements. According to trigonometric function theory, the synthesis of any periodic sine wave corresponds to a sine wave with a certain period; hence, it cannot have a unique phase difference center, as in the case of continuous spectrum band measurement. Therefore, it was necessary to mix multiple wavelengths and constrain the final common phase errors.

The analysis conducted in this study revealed that using dual wavelengths for light-intensity superposition and carrier waves can effectively enhance the measurement range. However, when the number of cycles is high, fluctuations in the light intensity may occur. As the optical frequencies become closer, the measurement range that can be covered increases. Based on the multiwavelength broadband measurement method and prior physical models, the effects of differences in multiwavelength envelopes and boundary blurriness on the center fringe positioning error were addressed. This was realized by considering factors such as the pixel resolution, fringe period, and other relevant parameters. Simultaneously, the sampling error owing to discontinuities in the light intensity was reduced, that is, the density of the fringes directly influenced the accuracy of the phase detection. Notably, finer and denser fringes resulted in more accurate phase measurements, because each fringe was the average of multiple fringes. In Fig. 2, the incident light of the collected optical path is parallel, which can be aimed at starlight or realized using a parallel light tube. Filters and lasers can be used to generate multiple wavelengths. Astronomical photonic devices are placed near the rear end of the pupil plane. As shown in Fig. 2, the two beams on different mirrors finally enter the rear end through the astronomical

photonics device for synthesis, thereby realizing the perception of a coherent state.

In the actual detection process, the higher the resolution of the fringe pixel, the higher is the phase detection accuracy. Moreover, by fitting with the standard fringe model in Eq. (2), the detection accuracy can be further improved. Fig. 2(a) shows the optical architecture of the large-aperture sparse telescope and the local optical path diagram for step phase difference detection. At the same time, a coupler is placed at the final receiving end to collect light passing through the edge of the submirror. By utilizing the characteristics of fiber coupling, only light from a smaller field of view is collected, thereby reducing the crosstalk between different fields of view. Fig. 2(b) shows the schematic diagram of multi-band measurement. It uses different wavelengths to achieve phase shift in the system, and obtains light intensity based on the local discrete sampling of the detector, thereby calculating the step phase difference.

The fringe pattern formed by the dual wavelengths exhibited irregularities at the boundaries, which were difficult to distinguish from stray fringes. Therefore, using combinations of multiple wavelengths, a prominent Gaussian distribution envelope can be formed to realize coarse co-phasing.

3 Results

3.1 Analysis of the system wavefront detection accuracy

Based on prior physical constraints, the reconstructed system parameters can be obtained by combining edge and multi-aperture detection. The entire wavefront of the system can be effectively reconstructed by fitting the rigid displacements at each subaperture position.

First, numerical simulations were performed to establish sparse aperture data with varying wavefront phase errors. The data were obtained based on the slope of the system, as measured by focal-plane interferometry. Considering the systematic wavefront reconstruction, the system adopted a limited number of edge measurements owing to its practical arrangement, resulting in a relatively low sampling rate.

Slope measurement is advantageous over absolute-height measurement because it offers a variable range, good accuracy compatibility, and high reconstruction robustness. Using slope data from multiple directions with varying sampling intervals and combining them with displacement measurement data of different accuracies, the slope measurements can be normalized to a common probability confidence level. Therefore, whether represented by internal measurement systems such as edge sensors or by external measurement systems such as wavefront sensing, a common reference can be established based on slope measurements, enabling a balance between accuracy and traceability. The relationship between the scale span and detection accuracy of both the internal and external telescope measurement systems is illustrated in Fig. 3. Diagonal curves can be constructed based on the square roots of the different slopes. As shown in the figure, the edge sensors exhibit a higher distance measurement accuracy owing to their close proximity. The use of laser ranging methods with larger distances in the formation of internal edge measurement systems results in an increased measurement distance.

In this study, the reconstruction algorithm error was analyzed. Based on the algorithm error, the edge detection error and detection noise must be superimposed to obtain the co-phase detection accuracy of the system. The final wavefront detection accuracy of the system directly affect the correction accuracy of the subsequent low-order aberrations of the system. For low-order phase differences, the co-phase errors obtained at each measurement point can be fitted using the modal method to reduce the random error of a single point.

Consequently, the absolute accuracy requirements of these systems were reduced. Moreover, for wavefront sensing, the larger the scale mapped onto the primary mirror, the lower are the absolute

measurement accuracy requirements. Thus, the obtained residual of the wavefront detection (reconstruction algorithm error) was better than 0.02 λ (λ = 1 550 nm). As shown in Fig. 3, the peak and trough values of the larger aberrations were approximately three operating wavelengths, and the peak and trough values of the smaller aberrations were approximately 0.05 wavelengths. Larger wavefront aberrations are dominated by low-order aberrations, such as coma and astigmatism, whereas smaller aberrations are dominated by spherical aberrations that are more difficult to adjust in the system.

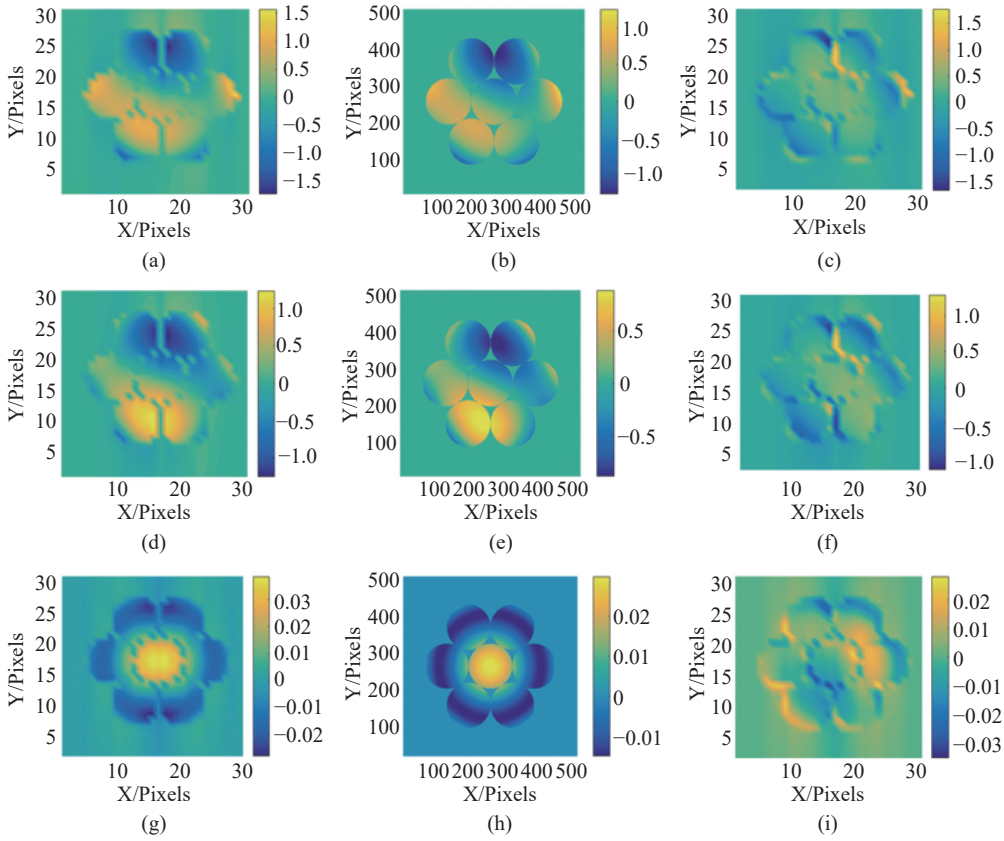

Fig. 3 Verification of the accuracy of the sparse aperture wavefront reconstruction. (a)–(c) Large aberration, (d)–(f) medium aberration, and (g)–(i) small aberration.

In practical measurements, the wavefront reconstruction of the system relies on slope measurements. Both the surface shape and slope of the mirror were obtained using the corresponding segmented subapertures. Considering the height differences obtained from the edge sensors and their spatial geometric models, the final calculated results were correlated with the slope measurements. The aperture sampling pattern adopted is shown in Fig.1(b). In this pattern, one subaperture uses two sampling points, whereas the other uses a single sampling point. Each sampling point was used to detect the step difference between two adjacent points on the opposite side and calculate the average step difference between them.

3.2 Experiment for feasibility verification

A coarse phase adjustment was achieved using the white-light interference principle based on broadband light interference. This study focused on a parallel multichannel high-throughput detection and resolution theory with the aim of reducing the modulation of fringe center positions introduced by the nonuniformity of various spectral channels. Considering dual-wavelength detection, the phase-parameter fitting method and the relationship between the combination of wavelengths, fringe period, and uniqueness of the central position were analyzed. For wavelength switching, the precise

synchronization mechanism of the high-throughput multimodal detection must be known.

The experimental setup is shown in Fig. 4. Light is initially coupled to optical fibers via a coupler, and multiple light paths are synthesized using lenses. A camera is used to capture images of the multipath fringes. The ultimate objective is to reduce the side lobes and blurring in the point spread function, while avoiding degradation of contrast and resolution. The system has an aperture of 450 mm and a focal length of 4.5 m (F = 10), which can effectively simulate long-focus systems. In the experiment, this system utilized 14 integrated interference modules (limited by the size of the fiber coupler and the caliber of the parallel light tube) and a camera at the back end to perform the parallel detection of its fringes. Compared with traditional physical optical components, the volume and weight of this system are significantly reduced. The total space occupied by the 14-beam integrated interference is less than 600 mm × 300 mm × 300 mm, which is more suitable for the tense focal plane space of future large-aperture telescopes, and can significantly reduce the launch weight of space telescopes.

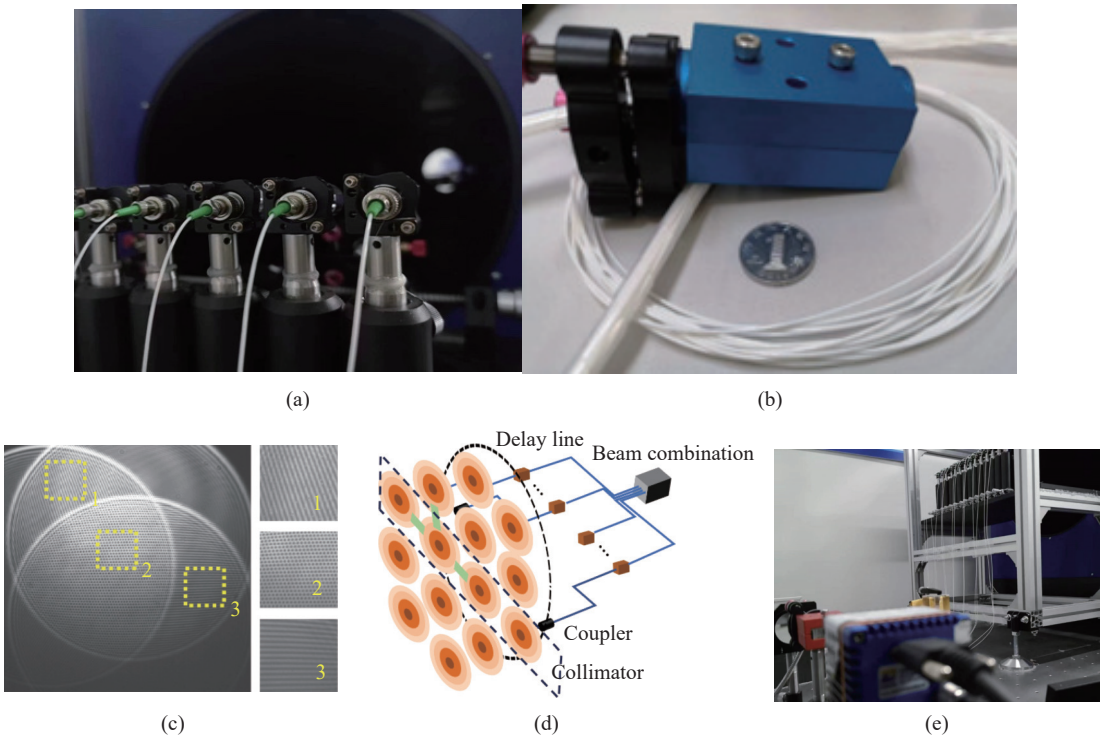

Fig. 4 Multilevel fringe tracking validation. (a) Linear array photon collection end, (b) integrated interference modules, (c) multilevel interference fringes, and (d) experimental set up diagram, (e) experimental optical layout picture

In the generation of incident light, a parallel light tube simulator can be used, where the main mirror of the parallel light tube is in the form of a parabolic mirror. Finally, a 14-channel detection is built on the system pupil plane.

According to the projection calculation of existing telescopes, this architecture can achieve the co-phase measurement of an 8-m telescope (14 apertures, single aperture 2-m in diameter; passive support for diameters below 2 m is very mature and only requires adjusting the position of the sub-mirror). This is merely a principal demonstration of the verification system. By further improving the integration, the same function can be achieved within a smaller range (100 mm × 30 mm × 30 mm). The traceability of measurement accuracy was derived from the accuracy of the single mirror used. According to the test report provided by the supplier, the emission accuracy of the light tube wavefront was better than 100 nm. Therefore, it was more suitable for detecting the common phase measurement process. In Fig. 4, the boxes in the figure represent the

sampling locations for the 14 apertures.

Thus, herein, "large-dynamic-range + high-resolution" fringe tracking validation was conducted based on the dual-wavelength principles. The interference fringes formed by narrowband light at 1 530 and 1 560 nm are shown in Fig. 5. Evidently, upon flat-field calibration and incoherent digital synthesis, the fringe contrast exceeded 0.4, its dynamic range exceeded 10 wavelengths at the operating center (1 550 nm), and the resolution outperformed one-tenth of the operating center wavelength (1 550 nm). The filters were used to generate narrowband beams at 1 530 and 1 560 nm. Through flat-field correction and beam combination of the two light intensities, a wide range of common phase adjustments can be realized. For the same physical interval δ, the fringe phases corresponding to different wavelengths have a certain difference $\Delta\Phi$, thereby achieving differential measurement in different channel spectra. The interference fringes generated in the different wavelength bands exhibit a phase difference.

$$2\pi\frac{\delta}{\lambda_1}-2\pi\frac{\delta}{\lambda_2}=\Delta\Phi \quad . \tag{4}$$

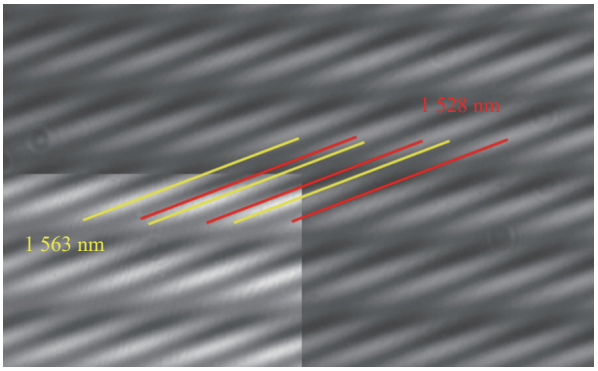

Fig. 5 Three-beam interference principle and its fringes in different wavelength ranges.

In special cases, when the fringes show the maximum change in the light and dark contrast, the relationship between the wavelength and actual physical interval can be directly obtained. Therefore, the channel spectrum method can be tested using broadband light or frequency sweeps.

According to Eq. (3), the intensity distribution of the system's fringes can be obtained, where the intensity distribution after wavelength phase shifting represents the situation along a certain interference direction.

$$I_1 = I_0 + A\cos\phi \quad , \tag{5}$$

$$I_2 = I_0 + A\cos(\phi-\Delta\Phi) = I_0 + A\cos\phi\sin\Delta\Phi - A\sin\phi\cos\Delta\Phi \quad , \tag{6}$$

$$I_3 = I_0 + A\cos(\phi+\Delta\Phi) = I_0 + A\cos\phi\sin\Delta\Phi + A\sin\phi\cos\Delta\Phi \quad , \tag{7}$$

Where I is the intrinsic light intensity, representing the sum of the light intensities of all paths, which can be obtained by measuring each path separately, and A is the amplitude of the fringes. The phase shift difference can be obtained by combining Eq. (5) ~ (7), as shown in Eq. (8).

$$\frac{I_2+I_3}{2} = I_0 + A\cos\phi\sin\Delta\Phi = I_0 + (I_1-I_0)\sin\Delta\Phi, \tag{8}$$

By transforming Eq. (8), we can get Eq. (9), and by combining it with Eq. (3), we can obtain the final step phase difference.

$$\Delta\Phi = \arcsin\left[\frac{I_2+I_3-2I_0}{2(I_1-I_0)}\right] \quad , \tag{9}$$

When the light and dark states of the system are reversed, the actual physical interval of the system can be directly obtained as follows:

$$\delta = \frac{1}{2}\frac{\lambda_2\lambda_1}{\lambda_2-\lambda_1} \quad . \tag{10}$$

Using the device depicted in Fig. 4, it was possible to achieve a spectral dispersion of varying widths, generating interference fringes within these different wavelength bands. The use of a detector array allows the acquisition of two-dimensional interference fringes. These interference fringes enable the derivation of slopes at the edges of the system, facilitating the inversion of the mirror pose and alignment conditions of the system. In addition, the two-dimensional variation in the light intensity of the system can be used to obtain the phase differences between each pair of the three light intensities

and simultaneously achieve the co-phasing measurement of the three paths. For sparse aperture boundaries, the phase differences between the three subapertures can be obtained simultaneously, and the overall control matrix can be constructed using the middle subaperture as a reference. Combined with the analysis results of Fig. 5, based on measuring the edge phase difference, equal-interval phase sampling was conducted at the main mirror position, which was used as the data source for the slope measurement. Using the overall solution model constructed in the theoretical analysis, we obtained the wavefront information of the entire system and achieved high-precision reconstruction. This further demonstrates the high integration and high-throughput advantages of astronomical photonics devices (for traditional physical optics measurement methods) in achieving high-density sampling of the system. It is necessary to enlarge the system pupil and place a corresponding number of collection optical paths. Simultaneously, for the system interference synthesis architecture, it is necessary to rearrange the optical path. According to Eq. (4), δ is 13.64 μm, and the bandwidth of a single wavelength is less than 0.2 nm. The interference fringes in the lower-left corner of the image are the result of another acquisition. The two are combined for ease of observation and comparison.

To utilize the fringes formed by white-light interference for coarse co-phase detection, the interference envelope of the dual wavelength was leveraged. This ultimately achieves coarse co-phase detection. Moreover, channel spectroscopy facilitates comparative measurements across various spectral channels, thus suppressing co-phase errors. Finally, for precise co-phase control of the system, experimental validation was conducted using two distinct approaches: (1) larger tilt angles and (2) smaller tilt angles. The outcomes of these approaches were experimentally demonstrated.

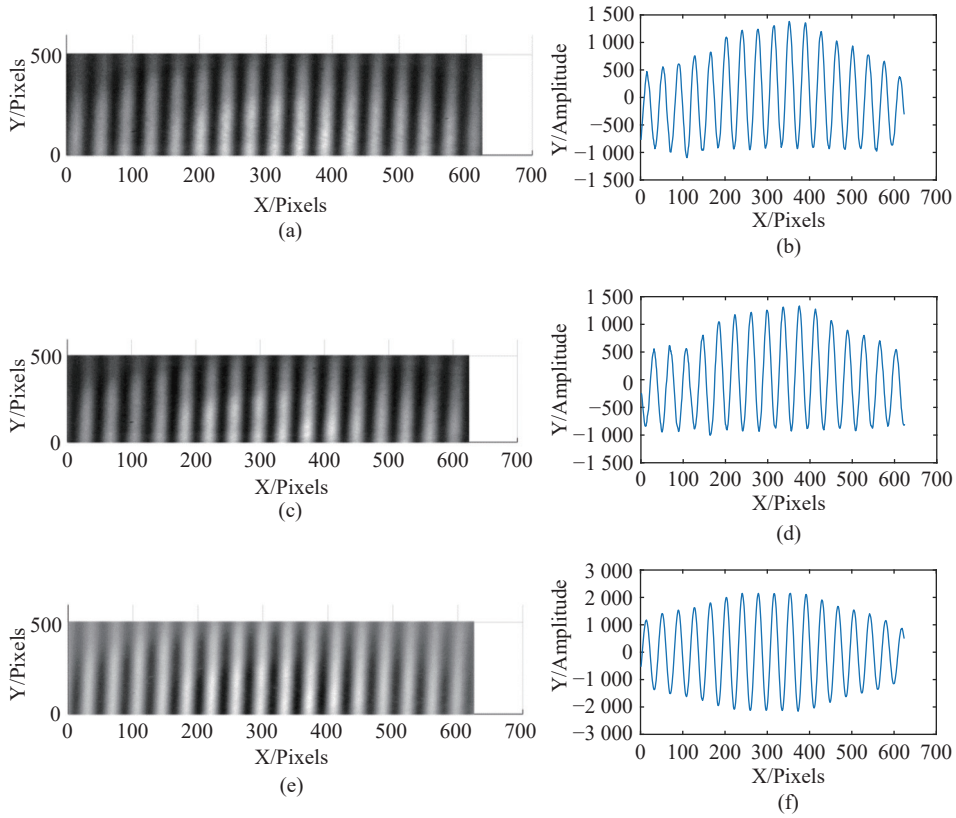

Fig. 6 Validation of the dual-wavelength fringe tracking. (a), (b) Interference fringes formed by the narrowband light at 1 530 nm and their average cross-section, (c), (d) interference fringes formed by the narrowband light at 1 560 nm and their average cross-section, (e), (f) incoherent synthesis of the dual wavelength and average cross-section.

For the segmented telescope, the co-phase of three mirrors was implemented in a laboratory environment. The segmented mirror multipath interference fringe tracking experiment is shown in Fig. 7. The co-phase error between the three paths can be obtained using the origin position. In this study, three hexagonal sparsely segmented mirrors with masks were used to simulate circular sparsely segmented mirrors.

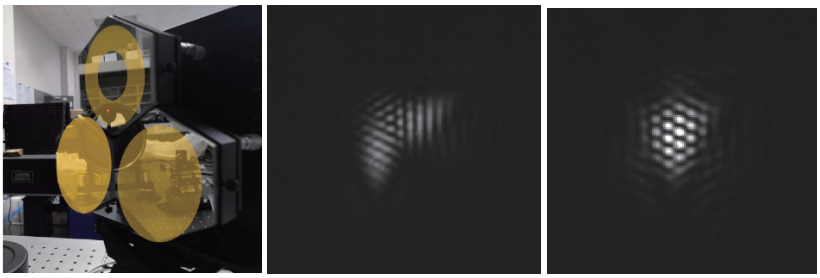

(a) (b) (c)

Fig. 7 Segmented mirror multipath interference fringe tracking experiment. (a) experimental system, (b) Three-path interference pattern, before correction, (c) Three-path interference pattern after correction.

By employing frequency-sweep measurements in both the C and L bands, the visibility of individual measurements can be enhanced, leading to an increased signal-to-noise ratio. This approach leverages the shifting and variation of the characteristic peak intervals corresponding to different frequency bands. After increasing the modulation speed, external noise can be effectively suppressed, and alternating carrier modulation can be employed to mitigate interference from the external environment. During the actual measurement process, a broadband approach was necessary to enhance the measurement range. Therefore, a frequency-sweep laser was used to generate the reference wavelength. Each interference cycle contained five pixels, resulting in a detection accuracy of 0.2 wavelengths.

4 Discussion

The proposed approach involves an optical fiber interconnect architecture that utilizes optical waveguides for photon collection and transmission, thereby overcoming the drawbacks of large spatial footprints and heavy weights associated with large-span optical apertures. To achieve sparse sampling of the emitted wavefront, which approximates the ideal wavefront, the phase errors of the system must be suppressed to enable a coherent synthesis. Fringe tracking technology is employed in response to the contrast degradation of interference fringes caused by factors such as environmental temperature fluctuations, vibrations, and bending during the actual detection process.

The mechanism for separating the low-contrast fringes from the stray fringes and noise was analyzed. The decoupling mechanism for the low-aberration design and additional aberrations during the co-focus control process were also evaluated. Furthermore, the evolution of the stability errors and the phase-shift compensation mechanism during exposure for long durations was elaborated. Through closed-loop control of the optical path differences, wavefront stability and, ultimately, coherent synthesis were achieved. In addition, this study elaborated on the distribution patterns of co-phase stability errors, elucidated the impact mechanisms of stability residuals on the optical performance of the system, and clarified the mechanisms for mitigating internal and external interface variations. By combining the experimental verification of local boundaries, statistical error validation, and large-scale boundary high-fidelity simulated extrapolation, this study investigated the error propagation of inherent design aberrations, submirror tilt, and submirror

curvature differences during the stable sensing and control process of an optical system. This includes the crosstalk between aberration (phase) and vignetting (intensity) errors. Finally, a novel framework for perceiving interface stability in large-aperture segmented mirrors was established, along with new guidelines for control to ensure stability.

Here, the boundary measurement was experimentally verified, and the application effect of the existing technology was analyzed by taking advantage of the aperture rearrangement of optical waveguides. In terms of flux calculation, traditional interferometry requires the construction of spectroscopic and beam-synthesis optical paths, and it is necessary to ensure that the distance between different optical paths is greater than the coherence distance. Photons are confined in waveguides by using photon astronomy methods, thereby achieving high-flux beam propagation and synthesis[21].

When the positions of the components shift, the optical path is altered and influenced by changes in the optical surface morphology. Consequently, this induces corresponding changes in the interference fringes. Pertinent information regarding the pose or position of the system can be obtained by interpreting and tracking the interference fringes. Similarly, this method can be used in systems requiring high phase accuracy and stability, such as space remote sensing cameras and high-precision optical microscopy equipment.

5 Conclusions

The proposed method has good application prospects for ground-based and space-based large-aperture telescopes. High functional integration and stability are urgently required for high-resolution, high-sensitivity, and high-contrast optical systems. Astronomical photonics provides innovative performance improvements in astronomical observations by leveraging the advanced technologies used in optical communications and interconnections. Through photon propagation, synthesis, and regulation in waveguides, crosstalk between channels can be effectively reduced, and more complex optical path arrangements can be realized. Using a fiber-interconnected system, a more flexible interference optical path was established with a programmable and modulable delay-line architecture. The astronomical photonic devices used included photonic couplers, optical fibers, and arrayed waveguide gratings (AWG). This integration level will be further improved in the future. This setup facilitated a flexible combination of different sampling positions and multiple interference paths. High-precision common-phase measurements were performed using multipath interference fringe tracking. The acquired wavefront detection residuals were superior to 0.02 λ (λ = 1 550 nm), and the co-phase range exceeded 7.9 μm. This system can simultaneously achieve three interference paths, thus resulting in a 50% improvement in the detection efficiency, based on which another mode of interference measurement was employed.

Acknowledgments.

Thanks Dr. Hu and Dr. Wang for the help in testing. We would like to thank Editage (www.editage.cn) for English language

Disclosures.: The authors declare no conflicts of interest.

References:

[1] SITARSKI B N, RAKICH A, CHIQUITO H, *et al*.. The GMT telescope metrology system design[J]. *Proceedings of the SPIE*, 2022, 12182: 1218207.

[2] MCLEOD B A, BOUCHEZ A H, CATROPA D, *et al*.. The wide field phasing testbed for the giant Magellan telescope[J]. *Proceedings of the SPIE*, 2022, 12182: 1218208.

[3] UMBRIACO G, VASSALLO D, FARINATO J, *et al*.. Deformable lens for testing the performance of focal plane

wavefront sensing using phase diversity[J]. *Proceedings of the SPIE*, 2022, 12185: 121856W.

[4] CATROPA D, MCLEOD B, D'ARCO J, *et al*.. Piston-tip-tilt mirror array in the wide field phasing testbed for the giant Magellan telescope[J]. *Proceedings of the SPIE*, 2022, 12185: 121854I.

[5] DEMERS R, BOUCHEZ A, QUIRÓS-PACHECO F, *et al*.. Phasing the segmented giant Magellan telescope: progress in testbeds and prototypes[J]. *Proceedings of the SPIE*, 2022, 12185: 1218518.

[6] YANG P Q, HIPPLER S, DEEN C P, *et al*.. Characterization of the transmitted near-infrared wavefront error for the GRAVITY/VLTI Coudé infrared adaptive optics system[J]. *Optics Express*, 2013, 21(7): 9069-9080.

[7] BONNEFOIS A M, FUSCO T, MEIMON S, *et al*.. Comparative theoretical and experimental study of a Shack-Hartmann and a phase diversity sensor, for high-precision wavefront sensing dedicated to space active optics[J]. *Proceedings of the SPIE*, 2017, 10563: 105634B.

[8] VOSTEEN L L A, DRAAISMA F, VAN WERKHOVEN W P, *et al*.. Wavefront sensor for the ESA-GAIA mission[J]. *Proceedings of the SPIE*, 2009, 7439: 743914.

[9] TRAUGER J, STAPELFELDT K, TRAUB W, *et al*.. ACCESS: a NASA mission concept study of an actively corrected coronagraph for exoplanet system studies[J]. *Proceedings of the SPIE*, 2008, 7010: 701029.

[10] LIOTARD A, BERNOT M, CARLAVAN M, *et al*.. Wave-front sensing for space active optics: rascasse project[J]. *Proceedings of the SPIE*, 2017, 10563: 105632W.

[11] CHEFFOT A L, PLANTET C, PINNA E, *et al*.. Differential piston sensing with LIFT: application to the GMT[J]. *Proceedings of the SPIE*, 2022, 12185: 1218557.

[12] HEDGLEN A D, CLOSE L M, HAFFERT S Y, *et al*.. First lab results of segment/petal phasing with a pyramid wavefront sensor and a novel holographic dispersed fringe sensor (HDFS) from the giant Magellan telescope high contrast adaptive optics phasing testbed[J]. *Proceedings of the SPIE*, 2022, 12185: 1218516.

[13] WILHELM R, LUONG B, COURTEVILLE A, *et al*.. Dual-wavelength low-coherence instantaneous phase-shifting interferometer to measure the shape of a segmented mirror with subnanometer precision[J]. *Applied Optics*, 2008, 47(29): 5473-5491.

[14] CODONA J L, DOBLE N. James Webb space telescope segment phasing using differential optical transfer functions[J]. *Journal of Astronomical Telescopes, Instruments, and Systems*, 2015, 1(2): 029001.

[15] ACTON D S, KNIGHT J S, CONTOS A, *et al*.. Wavefront sensing and controls for the James Webb space telescope[J]. *Proceedings of the SPIE*, 2012, 8442: 84422H.

[16] LI L L, ZHAO H T, LIU C, *et al*.. Intelligent metasurfaces: control, communication and computing[J]. *eLight*, 2022, 2: 7.

[17] LIU ZH, WANG SH Q, RAO CH H. The co-phasing detection method for sparse optical synthetic aperture systems[J]. *Chinese Physics B*, 2012, 21(6): 069501.

[18] CHEN ZH G, SEGEV M. Highlighting photonics: looking into the next decade[J]. *eLight*, 2021, 1: 2.

[19] SIROHI R. Shearography and its applications—a chronological review[J]. *Light: Advanced Manufacturing*, 2022, 3(1): 35-64.

[20] AN Q CH, ZHANG H F, WU X X, *et al*.. Photonics large-survey telescope internal motion metrology system[J]. *Photonics*, 2023, 10(5): 595.

[21] EISENHAUER F, PERRIN G, STRAUBMEIER C, *et al*.. GRAVITY: microarcsecond astrometry and deep interferometric imaging with the VLTI[J]. *Proceedings of the International Astronomical Union*, 2007, 3(S248): 100-101.